Effects of Trailing-Edge Synthetic Jet Actuation on an Airfoil

Omar D. Lopez Mejia*
University of the Andes, CO0001 Bogotá, Colombia
Robert D. Moser†
University of Texas at Austin, Austin, Texas 78705
and
Daniel P. Brzozowski‡ and Ari Glezer§
Georgia Institute of Technology, Atlanta, Georgia 30332

Experimental work has shown that tangential synthetic jet actuators close to the trailing edge are an effective way to trap and manipulate vorticity concentrations, leading to the modification of the aerodynamic properties of an airfoil. In the present computational study, a time-resolved detailed model is used to simulate the action of tangentially blowing synthetic jet actuators mounted near the trailing edge of a modified NACA4415 airfoil at a low angle of attack in order to provide detailed information about the flow and the modification of the aerodynamic properties of the airfoil. The main effect of the actuation on the time-averaged vorticity field is a bending of the separation shear layer from the actuator toward the airfoil surface. Similar to the experimental observations, full actuation of the suction side actuator increases the magnitude of the nosedown pitching moment and the lift force, while the pressure side actuator reduces the magnitude of the nosedown pitching moment and the lift force. While the actuation modifies the global pressure distribution, the most pronounced effects are near the trailing edge where a spike in the pressure coefficient is observed. The computed actuator effectiveness (measured by computing the increase/decrease of the aerodynamic properties of the airfoil) is in good agreement with experimental results, with discrepancies of less than 10%.

Nomenclature

α	=	angle of attack
c	=	airfoil chord
C_d	=	drag coefficient ($D/(1/2\rho U_\infty S)$)
C_l	=	lift coefficient [$L/(1/2\rho U_\infty S)$]
C_m	=	moment coefficient [$M/(1/2\rho U_\infty Sc)$]
C_p	=	pressure coefficient [$(P - P_\infty)/(1/2\rho U_\infty)$]
C_μ	=	momentum coefficient [$U_{\mathrm{rms}}^2 A_j/(1/2\rho U_\infty^2 S)$]
D	=	airfoil drag force
f_s	=	airfoil vortex shedding frequency
F^+	=	actuation Strouhal number based on chord ($\Omega c/U_\infty$)
L	=	airfoil lift force
M	=	airfoil moment at $c/4$
P_∞	=	freestream pressure
Re	=	Reynolds number based on chord ($U_\infty c/\nu$)
S	=	airfoil planform area
S_t	=	vortex shedding Strouhal number ($f_s c/U_\infty$)
T	=	convective time units (time U_∞/c)
U_∞	=	freestream velocity
ν	=	kinematic viscosity
ρ	=	density
Ω	=	frequency of actuation

*Assistant Professor, Department of Mechanical Engineering, Cra 1 Este No. 19A-40. Professional Member AIAA.

†Professor, Department of Mechanical Engineering, 204 East Dean Keeton Street.

‡Graduate Research Assistant, George W. Wooruff School of Mechanical Engineering, 801 Ferst Drive.

§Professor, George W. Wooruff School of Mechanical Engineering, 801 Ferst Drive.

I. Introduction

ONE of the flow control devices that is of particular interest to the aerodynamic research community is the synthetic jet actuator, which has been used in a variety of airflow flow control applications, such as separation control and modification of aerodynamic characteristics. During the 1990s, experimental work was focused on airfoil separation control at high Reynolds numbers with periodic excitation [1]. Seifert et al. [2] demonstrated that oscillatory blowing was an effective way to increase poststall lift by using a NACA0015 airfoil in several experiments in which a variety of parameters were changed, such as slot location, momentum coefficient, and excitation frequency [3]. It was shown that optimum performance was achieved for $F^+ \approx 1.0$, i.e., in the order of magnitude of the natural shedding frequency of the problem in question [4]. DeSalvo and Glezer, at the Georgia Institute of Technology, have shown that synthetic jet actuators are an effective way to enhance the lift and modify the pitching moment of wings and airfoils [5], and that effective control has been achieved with actuation frequencies an order of magnitude larger than the natural shedding frequency of the wake [6] so that these frequencies are decoupled. Glezer et al. demonstrated that high frequency control can be used to manipulate shear layers with a range of natural frequencies, causing an apparent modification of the aerodynamic shape of the lifting surface upstream of the separation point [7]. DeSalvo and Glezer [5,8,9] and DeSalvo et al. [10] showed that this type of control is an effective way to modify the aerodynamic properties of a lifting surface by manipulating the vorticity near the trailing edge by using a hybrid actuator that integrates a synthetic jet actuator into a small obstruction with a ramplike shape, giving the potential to replace conventional control surfaces such as flaps, spoilers, and deflectors [6].

Computational fluid dynamics (CFD) have played an important role in flow control problems of low-Reynolds-number aerodynamic applications, giving support and complementing the experimental work that has been done in the flow control research field. Regarding the simulation and modeling of synthetic jet actuators for flow control applications, it has been shown that the success in the simulation of a synthetic jet depends on a number of factors, including the turbulence model, the synthetic jet model, and the boundary conditions. Synthetic jet models used in the CFD community can be

grouped into three categories: detailed models, reduced-order models (ROMs), and periodic surface boundary condition models [11]. Detailed models resolve all the spatial and temporal scales of the synthetic jet actuator, and they are normally three-dimensional, although they can be simplified to two dimensions [11]. ROMs simplify the physics of the synthetic jet actuator and are suitable for many flow control applications; however, for tangential synthetic jet simulations, ROM models must include the jet–wall interaction, which can be difficult to model. Finally, a periodic surface boundary condition model is simply the application of a periodic inlet/outlet boundary condition at the synthetic jet outlet, without representing the details of the cavity [12].

The study presented in this paper is part of the Adaptive Vorticity Control Enabled Flight (AVOCET) project, the main objective of which is to design and build a closed-loop flow control system using synthetic jet actuators for flight maneuvering of small-scale unmanned aerial vehicles. Achieving this objective requires close interaction between experimental, theoretical, and computational efforts. This paper addresses the development and implementation of a detailed synthetic jet model to support the AVOCET research, focusing in particular on estimating the global aerodynamic forces on a NACA4415 airfoil, as modified by the actuators, and validating such models against existing experimental data. The development and implementation of CFD models for this synthetic jet application complements the experimental work done at the Georgia Institute of Technology, providing detailed information about the controlled flow. The experimental setup of the present study is described in Sec. II. Section III shows the computational tools (CFD code, turbulence model, mesh, and synthetic jet model) used in this study, and numerical results (including validation) are presented in Sec. IV.

II. Experimental Setup

The experimental setup for this study consists of an 18-in. chord-modified NACA4415 airfoil model with two tangentially issuing actuators mounted on the suction side (SS) and pressure side (PS) near the trailing edge. The entire model is installed in an open-return wind tunnel with a freestream velocity of 30 m/s, giving a $Re = 9 \times 10^5$. The actuators have a characteristic height of $0.017c$ and an effective jet outlet height of 0.4 mm, i.e., $8.5 \times 10^{-4}c$ [13]. The rms velocity at the synthetic jet outlet at full actuation, which is defined by the maximum excitation voltage that could be applied to the piezoelectric elements of the synthetic jet in the current experimental setup, is ≈ 40 m/s $= 1.333 U_\infty$. Figure 1 shows the difference between a NACA4415 (Fig. 1a) and the modified (Fig. 1b) version used as baseline for this computational study. The primary difference is in the trailing edge of the airfoil where the tangential synthetic jet actuators are mounted. In Fig. 1c, the dashed lines show the location of the PS and SS of the unmodified airfoil.

The diaphragm of the synthetic jet actuator consists of a metallic disk, attached to a piezoelectric element, placed in the lower side of the cavity. The actuators are excited with an oscillatory voltage input at an offresonance frequency of 2050 Hz [13], giving a Strouhal number based on the chord length of $F^+ \approx 31$. In the experiments,
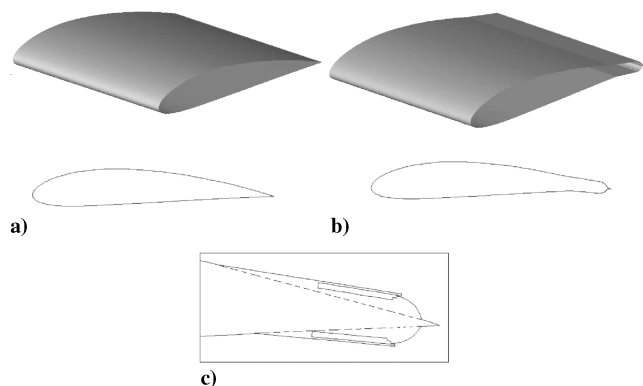
the momentum coefficient is $\mathcal{O}(10^{-3})$, and the Reynolds number based on the slot height and the rms velocity is $\mathcal{O}(10^3)$. There are 17 disks (each one located in a separated cavity) across the span on each side of the airfoil. The exit slots are segmented as the cavities in order to maximize jet exit velocity. The slot is continuous so that the discrete jets merge rapidly downstream of the exit orifice. The tangential synthetic jet actuator configuration used here is intended to control the concentration of vorticity formed close to the trailing edge [5,8,9]. The model also has 40 static pressure ports along the airfoil surface, and they are located in the midspan of the model [14].

For the measurement of the aerodynamic properties, a servomotor that is connected to the airfoil through a shaft (usually used for pitching motion) works as a moment transducer to indirectly measure the aerodynamic moment [15]. When the airfoil model is stationary, the aerodynamic pitching moment is equal to the externally applied torque (by the servo; i.e., T_{servo}) less the torque due to gravity (measured when the wind tunnel is off). The method may be extended to the case where the wing is dynamically pitching and plunging by incorporating measurements of an angular accelerometer; in which case, the unsteady aerodynamic pitching moment is given by

$$M = I_z \ddot{\alpha} - T_{\text{servo}} - T_{\text{grav}} \qquad (1)$$

where I_z is the rotational moment of inertia about the pitch axis, $\ddot{\alpha}$ is the angular acceleration, and T_{grav} is the torque due to gravity, which varies with the instantaneous angle of attack.

Two force sensors (one mounted on either side of the tunnel) measure the vertical forces that act on the model and are used to indirectly measure the lift [13]. When the airfoil model is stationary, the aerodynamic lift is equal to the vertical force (measured by the sensors; i.e., F_{sensor}) less the model weight (measured when the tunnel is off). The method may be extended to the case where the wing is dynamically pitching and plunging by incorporating acceleration measurements in plunge; in which case, the unsteady aerodynamic lift is given by

$$L = m\ddot{y} - F_{\text{sensor}} - W \qquad (2)$$

where m is the mass of the model, $\ddot{y}$ is the acceleration in plunge, and W is the model weight.

The wind tunnel is also equipped with a particle image velocimetry (PIV) system that includes a 100 mJ dual neodymium-doped–yttrium-aluminum-garnet (Nd:YAG) laser and two 1008×1016 pixel charge-coupled device (CCD) cameras [16]. Particle seeding is done with micron-sized smoke particles injected upstream of the model into the test section at a spanwise position aligned with the laser sheet [13]. The manufacturers and model numbers of the instrumentation used in this experimentation are listed next.

The PIV was measured by 1) a New Wave Solo PIV laser, 2) a Kodak MegaPlus ES 1.0 camera, 3) and LaVision DaVis 7.2 software. The static pressure was measured by a PSI NetScanner 98RK. The torgue and forces were measured by 1) a Baldor BSM100C–3150AA pitch servo, and 2) Transducer Techniques SBO-300 load cells.

III. Computational Tools

A. Computational Fluid Dynamics Code and Turbulence Model

For this computational study, an unstructured grid incompressible flow solver, called CDPv2.3,¶ was used as the basic CFD tool. CDPv2.3 was developed at the Center for Integrated Turbulence Simulations at Stanford University. This code uses a nondissipative large eddy simulation (LES) scheme, which is important for performing reliable turbulence simulations of incompressible flows. However, using LES in an aerodynamic application (such as this numerical study) can be expensive, particularly when close to the airfoil surface [17,18], which is why a hybrid Reynolds-averaged Navier–Stokes (RANS)/LES model, called delayed detached eddy

Fig. 1 Comparison between clean and modified NACA4415 airfoils.

¶This flow solver was named after Charles David Pierce, who was a professor at Stanford University.

simulation (DDES) [19], based on the Spalart–Allmaras (SA) equation, was implemented on CDPv2.3. The SA equation [Eq. (3)] is a convection–diffusion equation with source terms to control the generation and destruction of the model variable $\tilde{\nu}$:

$$\frac{\partial \tilde{\nu}}{\partial t} + \bar{U}_i \frac{\partial \tilde{\nu}}{\partial x_i} = c_{b1} \tilde{S} \tilde{\nu} + \frac{1}{\sigma} \left[\frac{\partial}{\partial x_i} \left((\nu + \tilde{\nu}) \frac{\partial \tilde{\nu}}{\partial x_i} \right) + c_{b2} \left(\frac{\partial \tilde{\nu}}{\partial x_i} \right)^2 \right]$$
$$- c_{w1} f_w \left(\frac{\tilde{\nu}}{d} \right)^2 \tag{3}$$

The first term on the right-hand side is a production term, the second term is a diffusive term, and the last term is a destruction term. The model variable $\tilde{\nu}$ and the eddy viscosity ν_t are related by $\nu_t = f_{v1} \tilde{\nu}$, where f_{v1} is given by

$$f_{v1} = \frac{\chi^3}{\chi^3 + c_{v1}^3} \tag{4}$$

In Eq. (4), χ represents the ratio of the model variable $\tilde{\nu}$ and the molecular viscosity ν; that is, $\chi \equiv \tilde{\nu}/\nu$.

$\tilde{S}$ in the production term of the SA equation is given by

$$\tilde{S} \equiv S + \frac{\tilde{\nu}}{\kappa^2 d^2} f_{v2} \tag{5}$$

where S is the magnitude of the strain rate tensor, d represents the distance to the wall, and $f_{v2} = 1 - [\chi/(1 + \chi f_{v1})]$. For the destruction term of the SA equation, f_w is given by

$$f_w = g \left[\frac{1 + c_{w3}^6}{g^6 + c_{w3}^6} \right]^{1/6} \tag{6}$$

where $g = r + c_{w2}(r^6 - r)$ and r is defined as $r \equiv \tilde{\nu}/\tilde{S}\kappa^2 d^2$. Finally, the constants that appear in Eqs. (4–6) are $\kappa = 0.41$ (Karman constant), $\sigma = 2/3$ (turbulent Prandtl number), $c_{b1} = 0.1355$, $c_{b2} = 0.622$, $c_{v1} = 7.1$, $c_{w1} = c_{b1}/\kappa^2 + (1 + c_{b2})/\sigma$, $c_{w2} = 0.3$, and $c_{w3} = 2$.

The DDES, as distinguished from standard detached eddy simulation (DES), consists of a redefinition of d as $\tilde{d}$ in the SA equation,

$$\tilde{d} = d - f_d \max(0, d - C_{\text{DES}}\Delta) \tag{7}$$

where $f_d = 1 - \tanh(8r_d)^3$, and r_d is given by

$$r_d = \frac{\tilde{\nu}}{\sqrt{U_{i,j} U_{i,j}} \kappa^2 d^2} \tag{8}$$

C_{DES} is a constant that is equal to 0.65, and Δ is a characteristic grid size commonly defined as the largest of the grid spacings in the three dimensions [i.e., $\Delta = \max(\Delta_x, \Delta_y, \Delta_z)$], but for an unstructured grid, Δ is normally defined as the diameter of the grid cell ϕ_{cv} divided by $\sqrt{3}$ [20]. This redefinition of d makes DDES behave like a RANS model in any part of the domain where $d \ll \Delta$ and as LES in the rest of the computation where $d \gg \Delta$. Futhermore, $\tilde{d}$ makes the interface between the RANS and LES regions (also called the gray region) very narrow, so that the transition between the two models happens more abruptly than in standard DES.

Results from early tests using DDES on separated flow showed unexpected high values of the eddy viscosity in the wake and in the separation region. To improve the performance of the turbulence model, an extended version of DDES (called EDDES [21]) was implemented. Figure 2 shows the eddy viscosity field from the DDES model and the EDDES model in a simulation of flow around a NACA4415 airfoil. A reduction of the magnitude of the eddy viscosity, of about one order of magnitude, is observed in the wake, accompanied by an stronger vorticity breakdown.

The main purpose of this extended version is to make quick transitions from RANS to LES modes outside of boundary layers by redefining Δ, f_{v1}, f_{v2}, and f_w as follows:
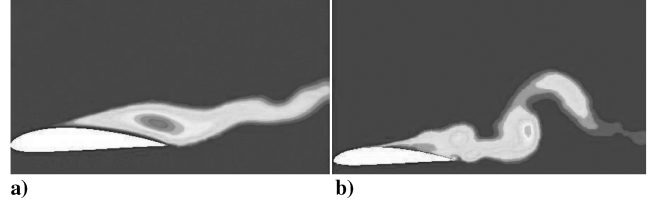

Fig. 2 Eddy viscosity field $\alpha = 30°$ and $Re = 5.7 \times 10^5$: a) DDES and b) EDDES.

Δ, f_{v1}, f_{v2} and

$$f_w = \begin{cases} \frac{\phi_{cv}}{\sqrt{3}}, \frac{\chi^3}{\chi^3 + c_{v1}^3}, \left(1 + \frac{\chi}{5}\right)^{-3} & \text{and} \quad g\left[\frac{1 + c_{w3}^6}{g^6 + c_{w3}^6}\right]^{1/6} & f_d < f_{d0} \\ \sqrt[3]{V_{cv}}, f_{v1} = 1, f_{v2} = 0 & \text{and} \quad f_w = 1 & f_d \geq f_{d0} \end{cases} \tag{9}$$

where f_{d0} is a threshold value for the function f_d, normally taken to be equal to 0.8, and V_{cv} is the volume of the cell.

1. Discretization of Spalart–Allmaras Equation in CDPv2.3

To be consistent with CDPv2.3, the discretization of the SA equation was done with the same kinetic-energy-conserving operators used in the Navier–Stokes solver [22]. In Eq. (3), as long as $\tilde{S}$ is positive, the destruction and production terms are always positive, so they may be treated as sources in order to preserve $\tilde{\nu}$ positivity. For the time advancement, a forward Euler scheme was also used to preserve the positivity of $\tilde{\nu}$; Backward Euler and Crank–Nicholson schemes were tested as well, but they lead to negative eddy viscosities, resulting in numerical instabilities. The discrete SA equation implemented on CDPv2.3 is given by

$$\frac{\tilde{\nu}^{n+1} - \tilde{\nu}^n}{\Delta t} + \text{conv}^{n+1} - \text{diff}^{n+1} = C_{b1}\tilde{S}^n\tilde{\nu}^n + \frac{C_{b2}}{\sigma}\left(\frac{\partial \tilde{\nu}}{\partial x_i}\bigg|^n\right)^2$$
$$- C_{w1} f_w^n \left(\frac{\tilde{\nu}^n}{\tilde{d}^n}\right)^2 \tag{10}$$

where the superscripts n and $n + 1$ indicate the time step. The discretization of the convective term conv^{n+1} is done with an upwinding scheme given by

$$\text{conv}^{n+1} = \sum_{f=1}^{n_f} \bar{U}_f^{n+1} \left[\left(\frac{\gamma \tilde{\nu}_{cv}^{n+1} + \beta \tilde{\nu}_{cv_{nbr}}^{n+1}}{2} \right) + \Phi \overline{\nabla \tilde{\nu}_{cv}}^n \cdot \hat{s} \right] A_f \tag{11}$$

The subscript cv stands for the control volume in which the equation is discretized; and the values of the coefficients γ, β, and Φ depend on the type of discretization used. By default, CDPv2.3 uses a second-order quadratic upstream interpolation for convective kinematics scheme in which $\gamma = 3/2$, $\beta = 1/2$, and $\Phi = 1$. $\bar{U}_f^{n+1}$ and A_f represent the averaged/filtered velocity normal to the face of the control volume and the area of the face, respectively. The diffusive term (diff^{n+1}) is given by

$$\text{diff}^{n+1} = \frac{1}{\sigma} \sum_{f=1}^{n_f} (\nu + \tilde{\nu}^n)_f \left[\psi \left(\frac{\tilde{\nu}_{cv}^{n+1} - \tilde{\nu}_{cv_{nbr}}^{n+1}}{\Delta s} \right) \right.$$
$$\left. + \overline{\nabla \tilde{\nu}_{cv}}^n \cdot (\hat{n} - \psi \hat{s}) \right] A_f \tag{12}$$

where $(\nu + \tilde{\nu}^n)_f$ is the sum of the molecular viscosity and the model variable evaluated at the face. Notice that the value of $\tilde{\nu}$ used in this case is at the old time level n to avoid nonlinearity of the diffusive term. $\overline{\nabla \tilde{\nu}_{cv}}^n$ corresponds to the average gradient of $\tilde{\nu}$ between the control volume and its neighbor (nbr). The variable $\hat{n}$ is the unit normal vector to the face f, and $\hat{s}$ is a unit vector defined in the direction from the centroid of the control volume to its neighbor. Δs is the distance between the centroid of the control volume and its neighbor. The variable ψ is a scaling factor that depends on
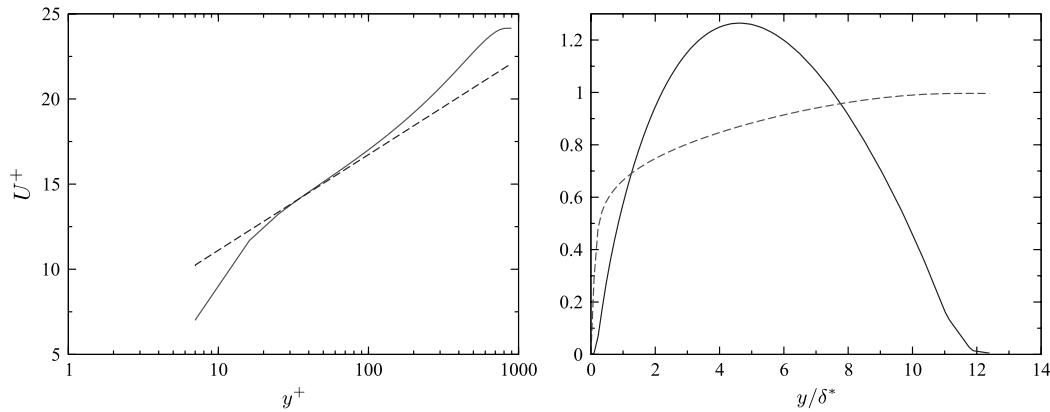
Fig. 3 Boundary-layer test results. On the left, the velocity profile is shown in wall units (solid line: DDES model; dashed line: log law). On the right, the dashed line denotes U/U_∞, and the solid lines denotes $\nu_t/(0.025U_\infty\delta^*)$ profiles.

geometrical parameters and, for unstructured grids, is defined as $\psi = \hat{s} \cdot \hat{n}$ [22]. The nonsymmetric sparse matrix that is obtained from the discretization of the SA equation is solved using a biconjugate gradient stabilized solver.

2. Extended Version of Delayed Detached Eddy Simulation Implementation Tests

EDDES implementation on CDPv2.3 was first tested with a flat-plate boundary layer, in which the model should behave like RANS since no separation is expected. In the wall normal direction, the first grid point is located at $y^+ = 6$, and a growing ratio of 1.2 was used from this point on; results were analyzed at $x = 1$, in which $Re_\theta = 6.6 \times 10^5$. Figure 3 shows U^+, eddy viscosity, and U/U_∞ profiles, in which the different regions of the boundary layer are clear, and a good agreement with the log law is appreciated.

The turbulence model implementation was also tested with a clean NACA4415 airfoil. A total of 11 simulations were performed for this test: nine of them were performed to validate the CFD code with legacy data, while the rest were intended to compare the results against experimental data obtained at the Georgia Institute of Technology and to test the performance of the EDDES implementation at a high angle of attack. The conditions for the first set of computational experiments were a wide range of angles of attack (−9 up to 12°) and $Re = 2.0 \times 10^6$. Figure 4 shows lift and moment (at quarter-chord) coefficient results along with legacy data for this airfoil [23]. In the region between $\alpha = -9°$ and $\alpha = 10°$, errors of less that 1% were found between the computational and experimental results. In this range, the turbulence model mostly behaves as a RANS model, since there is no massive flow separation. The slope of the C_l and C_m curves is well predicted by the numerical simulations. In the stall regime ($\alpha > 10°$), the wake is three-dimensional and computational results strongly depend on the spanwise domain extent [24].
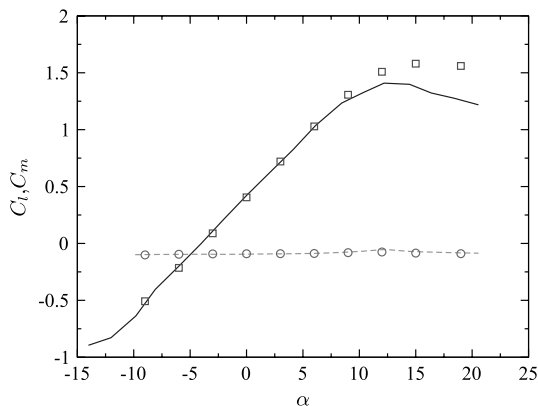

Fig. 4 NACA4415 computational and experimental [23] lift and moment coefficients (solid line: C_l exp, □: C_l comp, dashed line: C_m exp, ○: C_m comp).

Discrepancies of 20% between computational and experimental results at a high angle of attack have been observed when the spanwise domain extent is c, and better agreement was achieved with spanwise domains greater than $2c$ [24]. Shur et al. [25] suggest that at a moderate Reynolds number and angle of attack, the difference in the computational results and the aerodynamic properties of the airfoil between a $1c$ length domain and a $2c$ length domain in the spanwise direction is very small. Since this study is focused on low angle-of-attack simulations, it was decided that a $1c$ spanwise length is sufficient to achieve satisfactory results.

Two more tests at 19 and 30° with a $Re = 5.7 \times 10^5$ were performed to match the experiments at the Georgia Institute of Technology and to test the implementation of the turbulence model in a massively separated flow. Figure 5 shows the time-averaged vorticity field of the computational simulation (Fig. 5a) and a comparison with the experimental PIV data (Fig. 5b) [14]. Even though the experimental PIV data show smaller scales, with very strong vorticity in the separation bubble and missing data, the simulation and experiment are in good agreement regarding separation location (at $\frac{x}{c} \approx 0.3$) and the structure of the separation bubble.

Finally, Fig. 6 shows the time-averaged pressure coefficient as a function of $\frac{x}{c}$. The pressure coefficient plot is similar to the experimental one , with some small discrepancies in the peak pressure close to the leading edge and the pressure distribution on the SS of the airfoil.

B. Mesh

Any hybrid RANS/LES model requires an appropriate mesh, which plays an important role in the performance of the model. The criteria to design a mesh in DDES are based on physical and numerical arguments rather than on convergence issues (as is the case for RANS and DNS) [26]. Any mesh intended for a DDES model must have three basic regions: Euler, RANS, and LES. The Euler region is the zone in the computational domain in which irrotational flow is expected. For an external flow simulation, the Euler region covers the majority of the domain, especially upstream of the airfoil. The RANS region is the part of the domain that is close to the wall in which attached boundary layer is expected, and the guidelines to design it for a DDES simulation are exactly the same as those used in a pure RANS simulation. The LES region is the part of the computational domain (excluding the attached boundary layer) where substantial concentrations of vorticity and turbulence are expected. This region has an isotropic mesh with a characteristic grid size Δ_o, which is a measure of the LES filter. A hybrid C-type mesh was used in this study, since it allows a structured grid close to the airfoil (RANS region) and an unstructured grid in the rest of the domain (LES and Euler regions). A two-dimensional (2-D) view (XY) of the final shape and size of the mesh used here is shown in Fig. 7.

Based on $Re = 9 \times 10^5$ for a NACA4415 airfoil, a grid spacing of $\mathcal{O}(10^{-5}c)$ was chosen (for the RANS region) in the direction normal to the wall, so that the size of the first grid cell in wall units is about
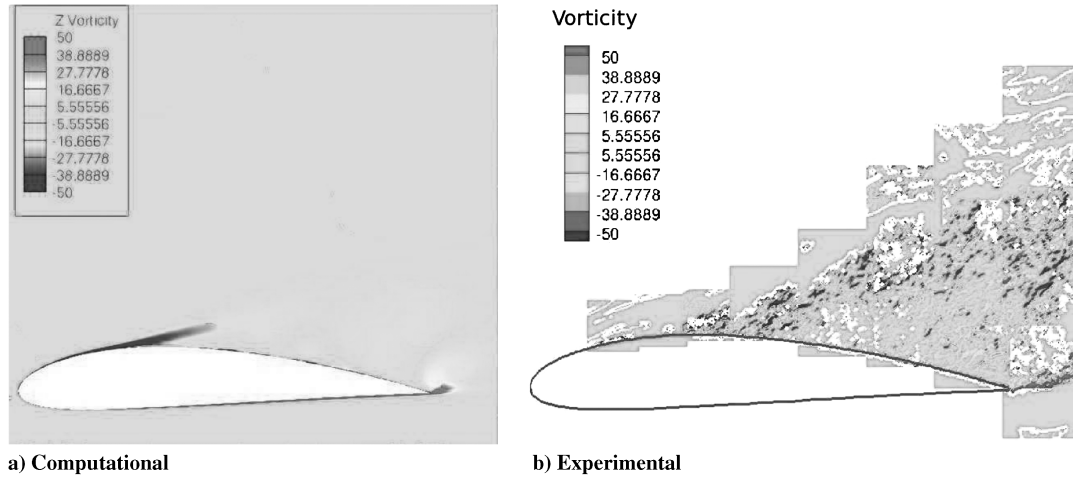
a) Computational   b) Experimental

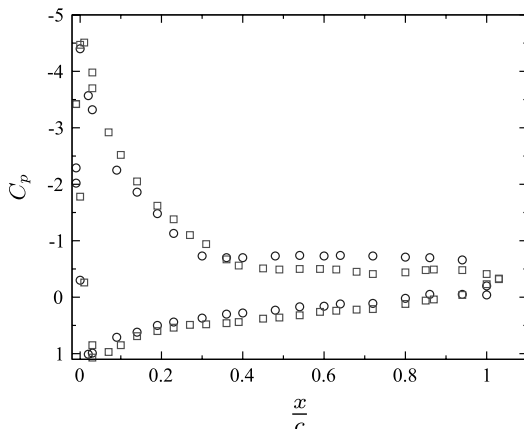**Fig. 5   Time-averaged spanwise vorticity for $\alpha = 19°$.**

Fig. 6   NACA4415 C_p as a function of $\frac{x}{c}$ at $Re = 5.7 \times 10^5$ and $\alpha = 19°$ (○: experimental, □: computational).

1.5; that is, $\Delta y_1^+ = 1.5$. Along the surface of the airfoil (streamwise direction), 150 grid points were used. These grid points were clustered toward the leading and the trailing edges, giving a grid spacing of $\mathcal{O}(10^{-2}c)$ to $\mathcal{O}(10^{-3}c)$. The stretching ratio used in the RANS region was 1.2, and the region was extended to about 3δ, where δ is the boundary-layer thickness, which was estimated with a combination of a vortex panel method and a numerical boundary-layer method for a flow over an unmodified NACA4415 airfoil at $\alpha = 3°$. The LES region is probably one of the most important parts of the domain, because it is the region in which the dynamics of the wake are resolved and a parabolic geometry was chosen for this

Fig. 7   XY view of computational domain.

region (see Fig. 8a). Fifty grid points were used in the spanwise direction determining $\Delta_o = 0.02c$. The LES region mesh was generated so that most of its elements were isotropic with an edge size of $\approx \Delta_o$. Finally, the Euler region covers the rest of the domain and has a characteristic mesh size of $0.1c$. Figure 8 shows the final mesh used in this research, including a detail of the mesh (see Fig. 8b) in the RANS region and the transition from structured to unstructured. Gridgen, a commercial software package for grid generation, was used to generate the grid used in the present study. The mesh was created by blocks, taking advantage of the automatic mesh generators and smoothness algorithms available in Gridgen. The blocks in the RANS and the viscous LES regions were created first. Based on these blocks, the focus region was generated and, finally, the Euler and departure regions were created. To build the three-dimensional domain, all the blocks were extruded in the z direction. A Gridgen script file** can be used to recreate this process and the mesh used in this numerical study. To execute this script, a grid file,†† which describes the modified NACA4415 geometry, is required. The boundary conditions used for this mesh were periodicity in the spanwise direction, nonslip over the airfoil surface, and free boundary conditions at the remaining boundaries.

C.   Synthetic Jet Model

The synthetic jet model used in this study consists of resolving the spatial and temporal details of the synthetic jet by imposing a 2-D inflow/outflow boundary condition on one of the cavity walls. Although the cavity deformation is not modeled, zero net mass flux is enforced. To simulate the diaphragm oscillation, a specified normal velocity given by

$$U_n = A \sin 2\pi F^+ T \qquad (13)$$

was imposed on the left boundary of the cavity (see Fig. 9). In Eq. (13), A represents the amplitude of the boundary condition, and it is determined by the rms experimental velocity at the synthetic jet outlet. The value of A used in this study was $0.38U_\infty$, giving a computed rms velocity at the synthetic jet outlet of about $1.3U_\infty$. Here, F^+ was set to 31.2, which corresponds to a frequency of 2050 Hz. The time step used in this model was $3 \times 10^{-4}c/U_\infty$ to ensure ≈ 100 samples per actuation cycle. This constraint in the time-advancing limits the Courant–Friedrichs–Lewy number to ≈ 9.

Previous research on synthetic jet simulation using incompressible Navier–Stokes solvers has shown that the size of the cavity does not play an important role in determining the characteristics of the synthetic jet [11]. In the dynamics of the flow in a synthetic jet, not
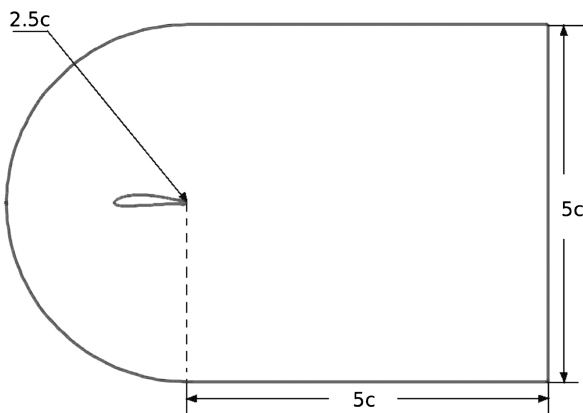

**Data available at http://turbulence.ices.utexas.edu/data/gridgen_avocet/ modifiedNACA4415.glf [retrieved 1 June 2009].

††Data available at http://turbulence.ices.utexas.edu/data/gridgen_avocet/ modifiedNACA4415.grd [retrieved 1 June 2009].

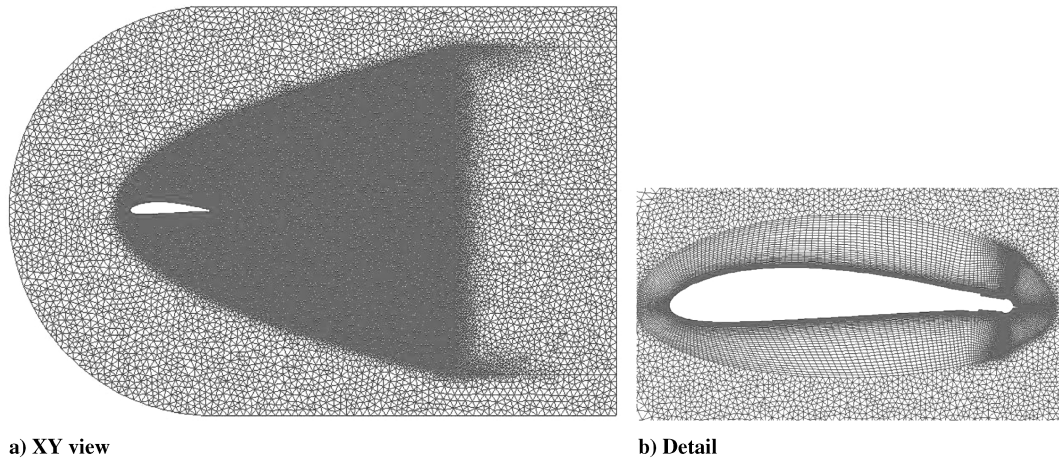a) XY view   b) Detail

Fig. 8   Computational mesh showing various domains required for DDES.
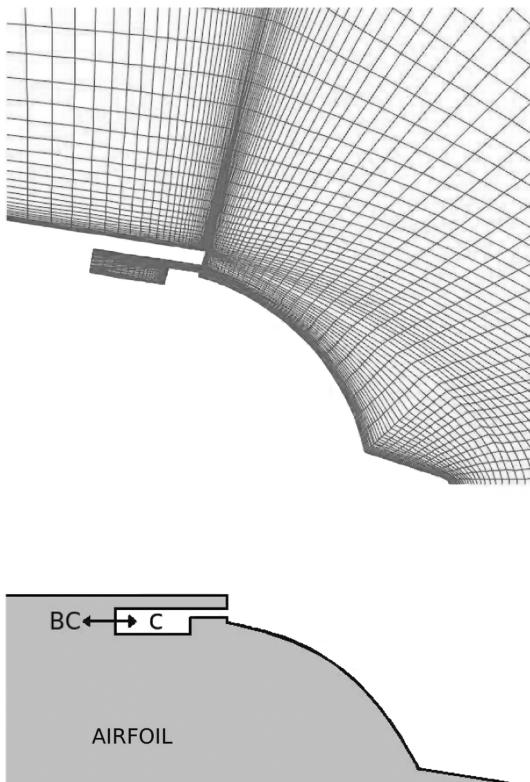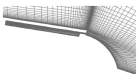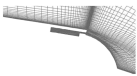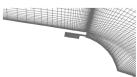

Fig. 9   Geometry of synthetic jet cavity (c) with mesh and detail of the
boundary condition (BC).

**Table 1   Different cavity sizes and moment coefficients
at $\alpha = 0°$; $Re = 9 \times 10^{5}$[a]**

Cavity	Volume, cm^3	C_m noact	C_m SSact	C_m PSact
	1.2	−0.088	−0.1029	−0.0675
	0.6	−0.089	−0.1021	−0.0678
	0.3	−0.089	−0.1031	−0.0681

[a]. The term noact denotes no actuation, SSact denotes SS actuation, and PSact
denotes PS actuation.

only its outlet is important but also the small channel that connects
the cavity to the synthetic jet outlet [12]. Based on these observations
and on the actual design of the synthetic jet, the exact dimensions of
the synthetic jet outlet and channel were used, while the size of the
cavity was reduced. Several computational experiments performed
with different cavity sizes showed that the effect on the aerodynamic
properties of the airfoil was negligible (See Table 1). Finally, the size
of the cavity used in the model is about four times smaller than the
actual cavity used in the experiments. A smaller cavity size reduces
the computational time required for the solution of the Navier–
Stokes equations and reduces the complexity of the boundary
conditions inside the cavity.

IV.   Numerical Results

Computational results are primarily focused on the spanwise
vorticity field close to the trailing edge, as well as in the integrated
aerodynamic properties: in particular, the lift C_l and moment C_m
coefficients. For validation, numerical results of the spanwise
vorticity field are compared against PIV measurements. The flow
over the airfoil is characterized using phase-locked PIV in the cross-
stream plane $z = 0$. The flow is seeded with micron-sized smoke
particles (using a commercial fog machine, where the nominal
particle diameter d is 50 μm) and is illuminated using a double-pulse
Nd:YAG laser. Image pairs are captured using a 1008×1016 pixel
CCD camera that is mounted on a two-axis (computer-controlled)
traversing mechanism. For each actuation condition, 200 image pairs
were obtained at a spatial resolution of 130 μm/pixel. The
uncertainties in PIV measurements are based on the analysis of
Adrian [27] and Westerweel [28]. The time-averaged velocities have
an estimated uncertainty of less than 0.5%.

A.   Baseline Case (No Actuation)

Several static cases of the modified NACA4415 airfoil without
actuation were performed; for these simulations, the Reynolds
number was fixed at 9×10^5 and the angle of attack was varied from 0
up to 15°. Figure 10 shows a comparison between the experiments
and the computational simulation of the time-averaged spanwise
vorticity close to the trailing edge at $\alpha = 0°$. Even though there is not
a good general agreement in the vorticity field, some features of the
flow, such as the magnitude of the vorticity, the thickness of the shear
layer formed at the end of the actuator ramp, and the size of the
recirculation regions formed downstream of the trailing edge, are
fairly well captured in the numerical results. An observable differ-
ence is that the computational results show stronger concentration of
vorticity close to the airfoil surface. This difference can be attributed
to the higher resolution of the CFD model close to the airfoil
compared with the PIV measurements. The number of grid points in
this region in the CFD model is about an order of magnitude greater
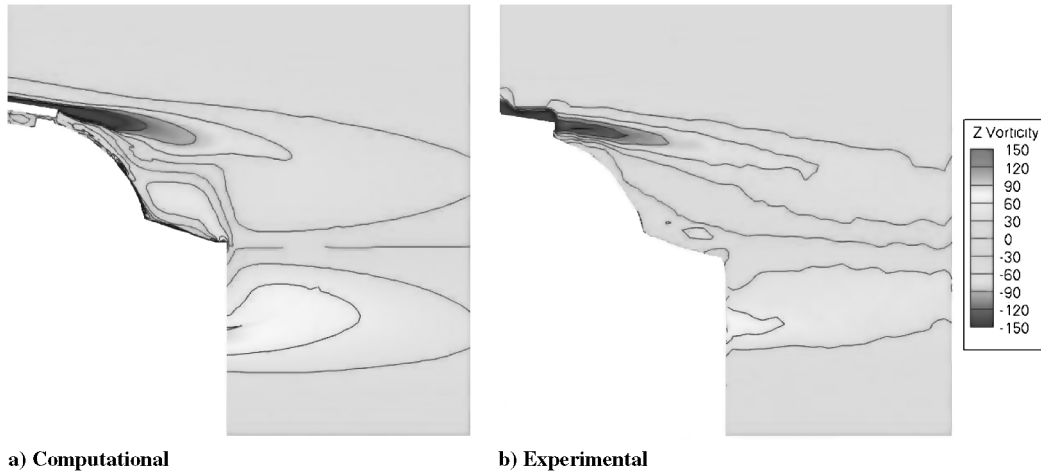than the highest PIV measurement resolution.

a) Computational   b) Experimental

Fig. 10   Averaged spanwise vorticity modified NACA4415 for $\alpha = 0°$.
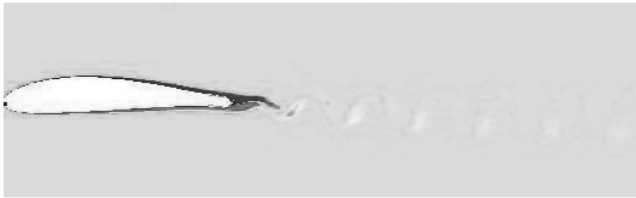

Fig. 11   Instantaneous and spanwise-averaged vorticity field (bottom) at $Re = 9 \times 10^5$ and $\alpha = 0°$ (modified NACA4415).

The instantaneous (spanwise averaged) vorticity field shows a clear vortex street in the wake, in which the distance between vortical structures is $\approx 0.24c$ (see Fig. 11). Numerical results showed $S_t = 4.2$, which has an error of approximately 7% with respect to the experimental Strouhal number [13].

Figure 12a shows the lift and moment coefficients with an average error of less that 3% with respect to the experimental results. For the pressure drag coefficient (Fig. 12b), there is an average error of 12% between the computational and experimental results, which is expected, since drag prediction with CFD is a difficult task. The C_l curve slope is slightly underpredicted by the CFD model, and the C_m curve in the experiments is flat, while in the computations, the slope is slightly negative.

Figure 13 shows a comparison of the computational results between the unmodified and modified NACA4415 profiles. While the C_l curve slope is not strongly influenced by the geometrical modification of the airfoil profile, there is a radical change to the C_m curve slope. Changes in $\partial C_m / \partial \alpha$ have been observed experimentally by DeSalvo and Glezer [8] with similar actuators but on a different airfoil section. An important numerical parameter that can be computed from these results is $\partial C_m / \partial C_l$ at a low angle of attack, which is related to the location of the aerodynamic center of the wing section. For the unmodified case $\partial C_m / \partial C_l \approx 0.0035$, so that the aerodynamic center is located at $x_{ac}/c \approx 0.245$, which is very close to the experimental result of 0.242 [23]. In the modified case $\partial C_m / \partial C_l \approx -0.022$, meaning that the aerodynamic center is located at $x_{ac}/c \approx 0.272$. Based on these calculations, the aerodynamic center moved toward the trailing edge due to the geometrical modification of the airfoil section.

Figure 14 shows the pressure coefficient for both the unmodified and modified NACA4415. A modification of the pressure distribution along the airfoil surface is observed for $x/c > 0.7$ due to the actuator. There is a reduction of the pressure along the actuator ramp (due to a flow acceleration), and the pressure close to the trailing edge is reduced due to flow separation.

B.   Actuated Case
1.   Effects on Vorticity Field

Figure 15 shows the time-averaged vorticity contours close to the SS actuator, in which it is clear that the average effect of the synthetic jet is to bend the shear layer (formed at the end of the actuator ramp) toward the actuator surface. This bending of the shear layer has been observed experimentally (see Fig. 16) and is associated with lift enhancement due to a local reduction of the pressure [13]. While the details of the near actuator mean streamlines are a bit different in the experiments and computations, the amount by which the extend streamline deflected is about the same. Another important change brought on by the actuation is the strength of the trapped vorticity close to the trailing edge. But, as in the unactuated case, the computational results show more vortical structures in this region than the experimental PIV data.
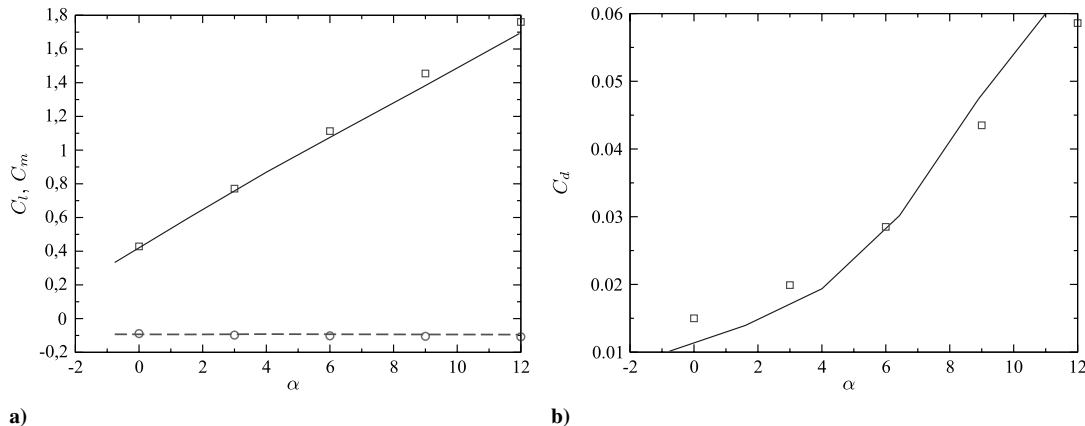

a)   b)

Fig. 12   Lift, moment, and pressure drag coefficients for modified NACA4415 ($\square$: C_l, C_d comp, solid lines: C_l, C_d exp, dashed lines: C_m exp, $\bigcirc$: C_m comp).
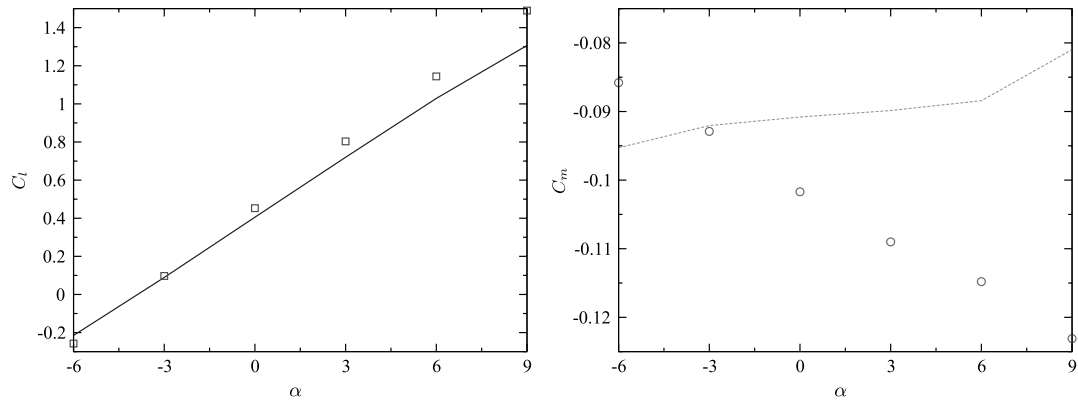
Fig. 13 C_l and C_m vs α for the NACA4415 airfoil (computational results) (solid line: C_l unmodified, $\square$: C_l modified, dashed line: C_m unmodified, $\bigcirc$: C_m modified).
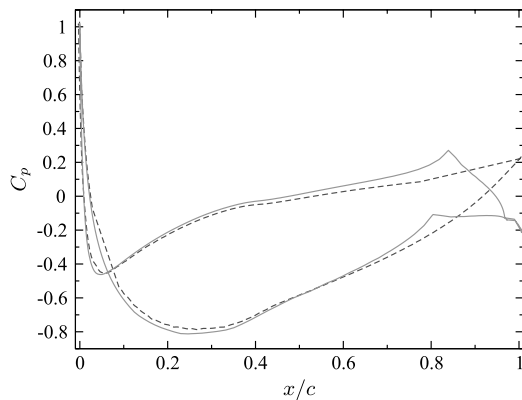

Fig. 14 C_p comparison for the NACA4415 airfoil at $\alpha = 0°$ (dashed lines: unmodified, solid lines: modified).

Figure 17 shows the time-averaged vorticity field in the near wake with either the SS or the PS actuators activated. The symmetry of the recirculation regions in the near wake shown in the unactuated case (see Fig. 10) is lost. It is shown as a downwash and an upwash of the near wake for the suction and PS actuation, respectively, which are consistent with the experimental PIV results shown in Fig. 18 [16].

The effect of the actuators on the wake is more dramatic in the instantaneous vorticity fields. Figure 19 shows the instantaneous (spanwise-averaged) vorticity field of the wake for the SS actuation (Fig. 19a) and the PS actuation (Fig. 19b) at $15T$ after the actuation was initiated. Numerical results show that, for the SS actuation, the Strouhal number increases to 5.1, as was corroborated through a Fourier analysis. It is also clear that the wake for the SS actuation is thinner in comparison with the unactuated case (see Fig. 11). On the other hand, the PS actuation produces a different effect on the wake; it reduces the vortex shedding substantially, and a stabilization of the wake is observed after $8T$. Attenuation of vortex shedding with high
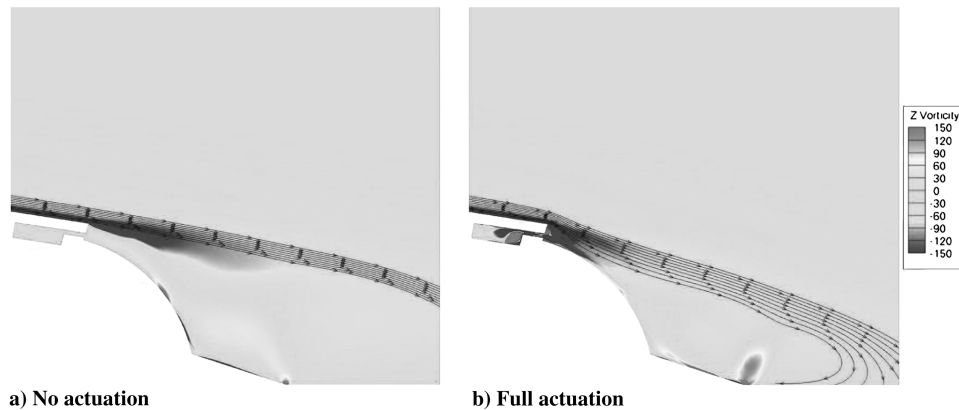

a) No actuation   b) Full actuation

Fig. 15 Time-averaged vorticity field for SS actuator (computational results).

a) Computational   b) Experimental
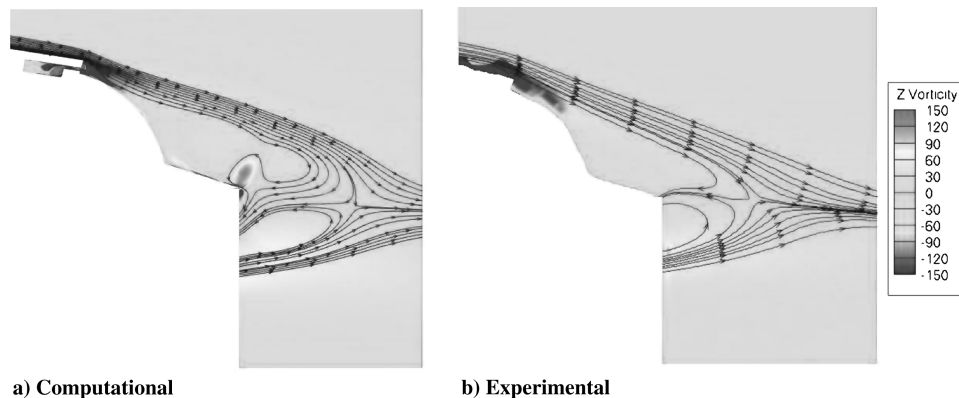
Fig. 16 Time-averaged vorticity field including streamlines for SS actuator.

frequency actuation has also been observed in other experimental studies, in which it was found that the high frequency actuation increases the dissipation and reduces the turbulent kinetic energy in the wake [7].

Numerical experiments showed that the stabilization of the wake was broken if the trailing edge was rounded with a radius of $\approx 0.001c$. Figure 20 shows the effects of the rounding in the instantaneous and time-averaged vorticity for the PS actuation. It is clear that the time-averaged vorticity shows a shorter near wake and the instantaneous vorticity field shows a vortex street.

2. Synthetic Jet Formation

Figure 21 shows the evolution of the vorticity and velocity vector field in one actuation cycle at full actuation. The cycle starts with the inflow phase (Fig. 21a). In this stage, the fluid is sucked into the actuator cavity; as this is happening, a clockwise vortex is formed over the synthetic jet outlet. The size and strength of the vortex increases as the inflow finishes, as is shown in Fig. 21b. The outflow phase starts in Fig. 21c; at this moment, the fluid that is blown out of the cavity interacts with the clockwise vortex and detaches it. As the outflow continues, a counterclockwise vortex (Fig. 21d), which is
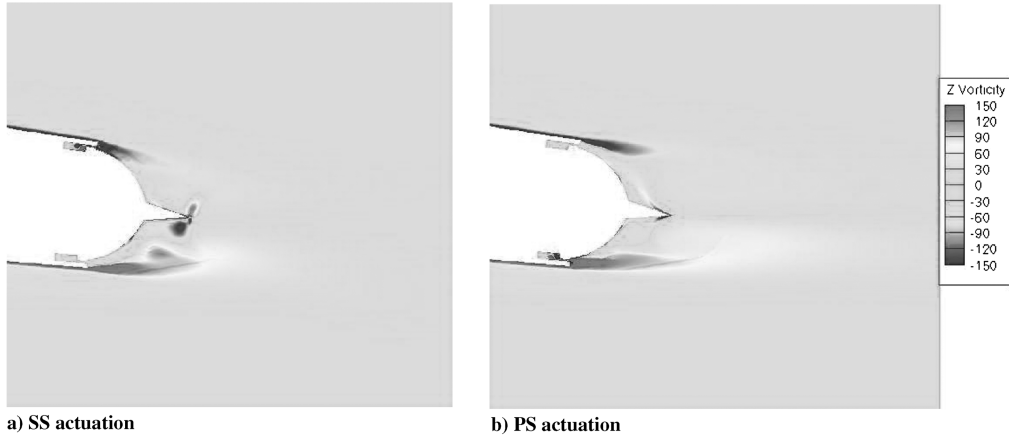

a) SS actuation   b) PS actuation

Fig. 17 Computational time-averaged vorticity field in the near wake ($\alpha = 0°$).

a) SS actuation   b) PS actuation
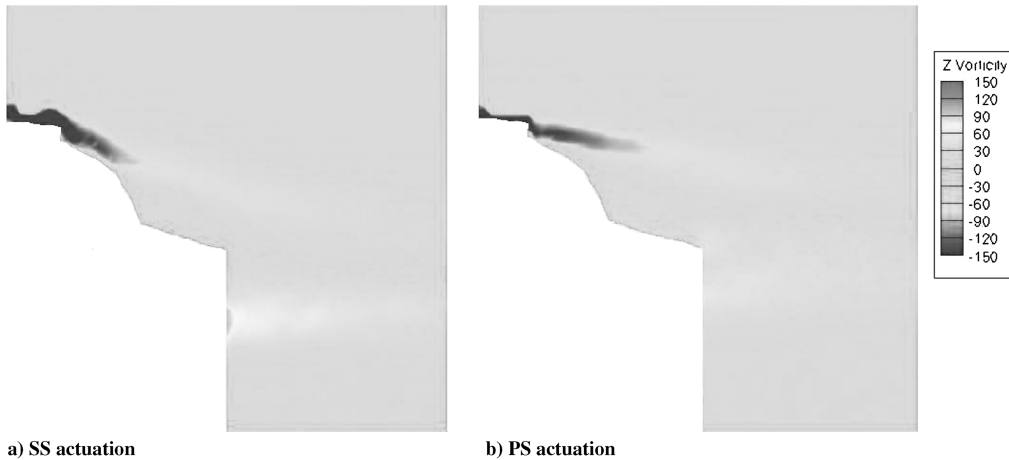
Fig. 18 Experimental time-averaged vorticity field in the near wake ($\alpha = 0°$).

a) SS actuation   b) PS actuation
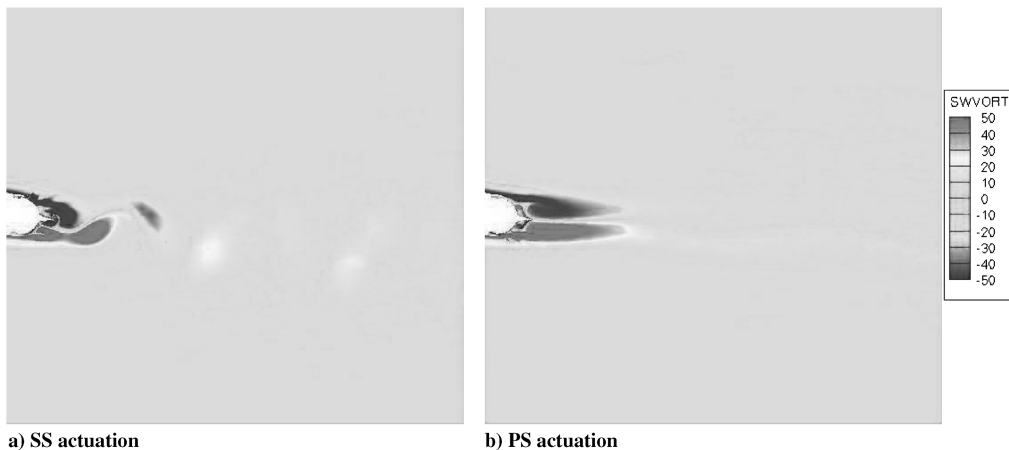
Fig. 19 Instantaneous vorticity field in the wake ($\alpha = 0°$).

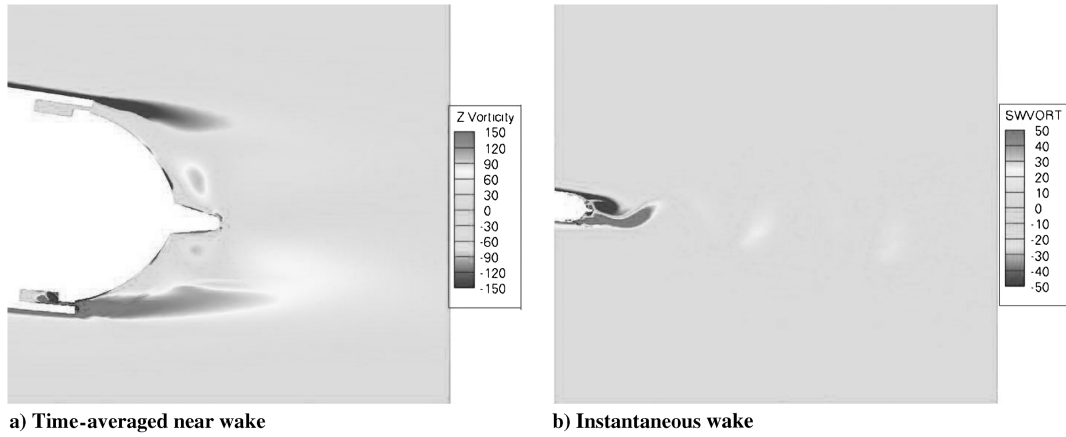a) Time-averaged near wake

b) Instantaneous wake

Fig. 20   Vorticity field for the rounded trailing-edge case (PS actuation and $\alpha = 0°$).
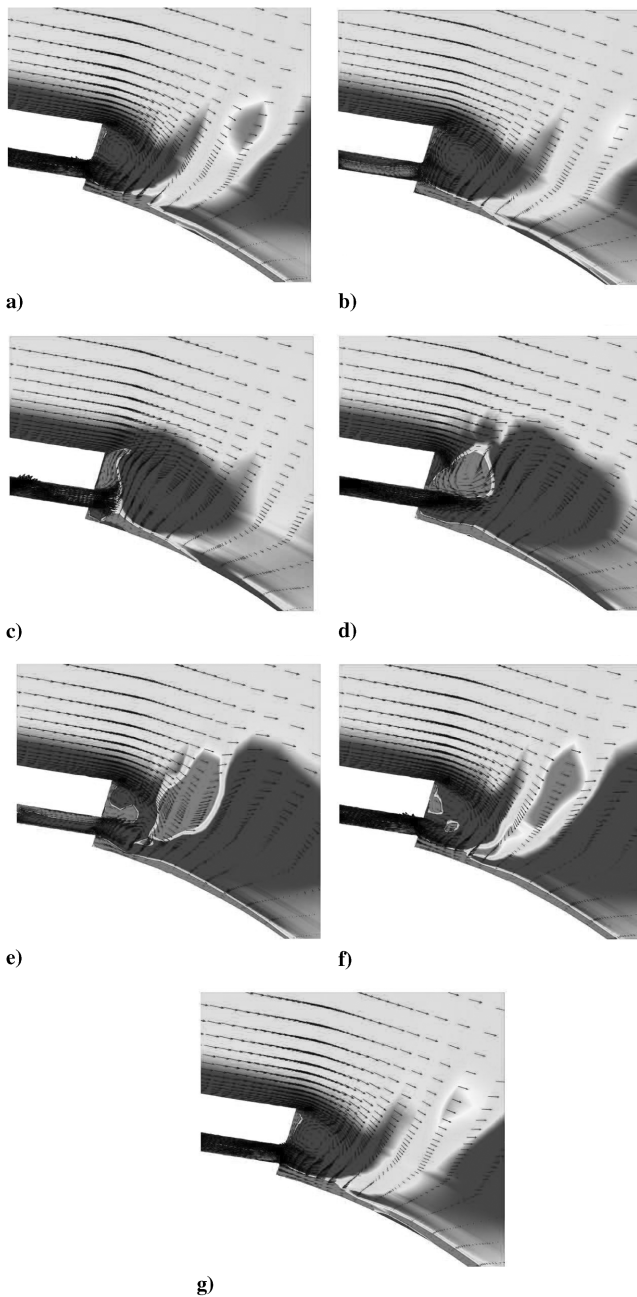

a)

b)

c)

d)

e)

f)

g)

Fig. 21   Evolution of vorticity and vector field close to synthetic jet outlet for full actuation and several phase angles θ of a) 1.5π, b) 1.75π, c) $2\pi = 0$, d) 0.5π, e) π, f) 1.25π, and g) 1.5π.

a)

b)

c)

d)

e)

f)

g)
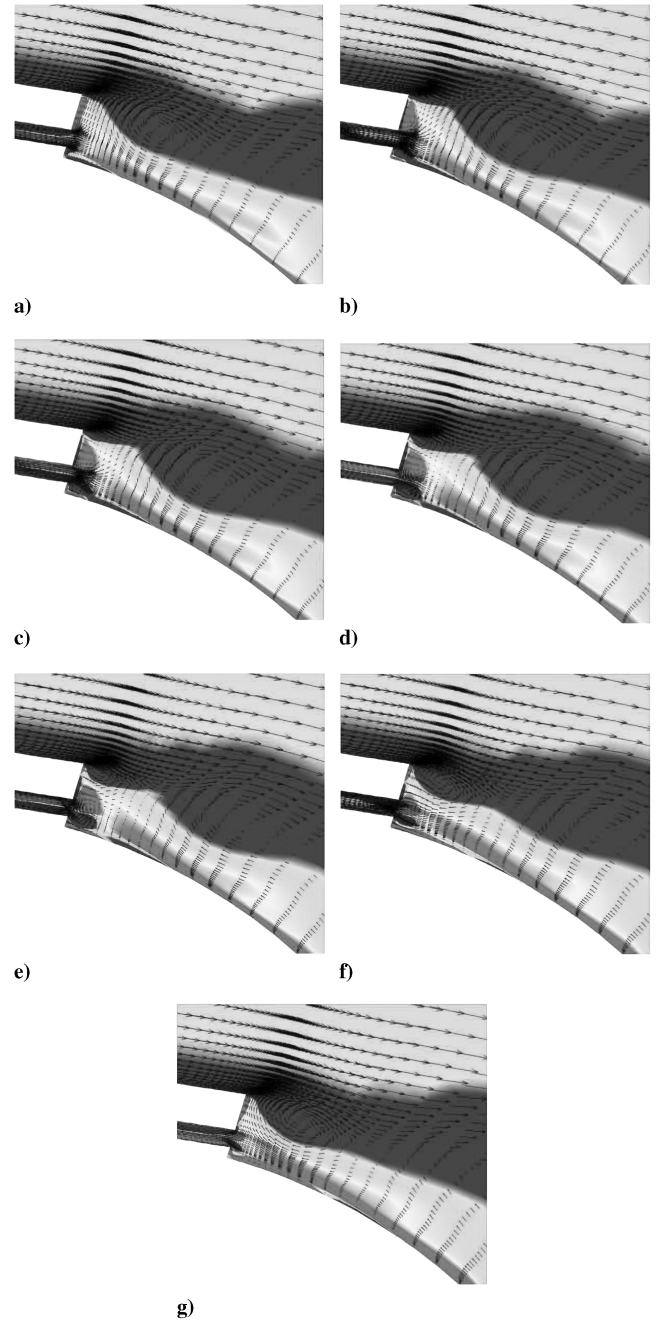
Fig. 22   Evolution of vorticity and vector field close to synthetic jet outlet for one-quarter of full actuation and several phase angles θ of a) $0 = 2\pi$, b) 0.5π, c) π, d) 1.25π, e) 1.5π, f) 1.75π, and g) 2π.
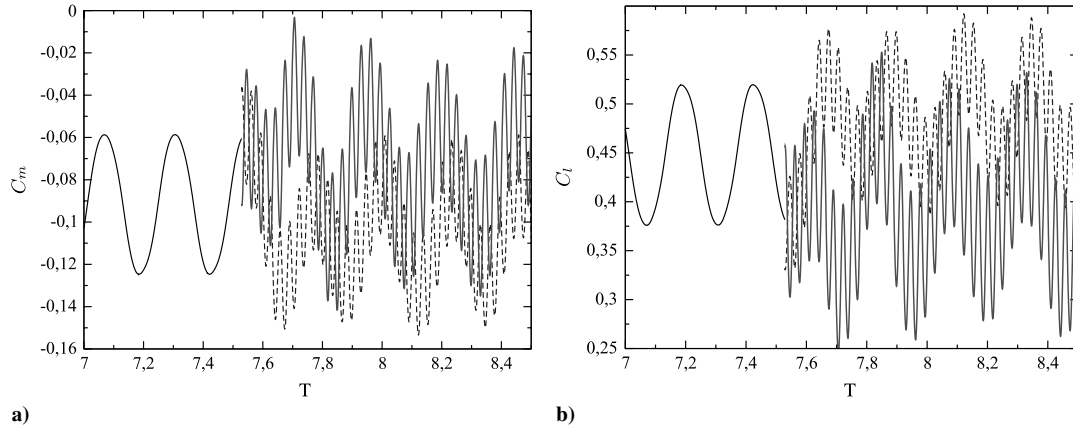
Fig. 23 Evolution of aerodynamic properties (solid line: no actuation, dashed line: SS, solid line: PS).

smaller and weaker than the clockwise vortex of the inflow phase, is created at the synthetic jet outlet. Figure 21e shows the end of the outflow phase, where the counterclockwise vortex detaches from the actuator due to the crossflow. Both vortices interact with the wall vorticity and with the shear layer as they are convected downstream. Figure 21f shows the beginning of the inflow stage, in which the clockwise vortex starts. Finally, the cycle is completed, as shown in Fig. 21g.

The dynamics of the vorticity field at the synthetic jet outlet depend on a formation criterion, which is a function of the inverse of the Strouhal number based on the slot height (F_h^+):

$$\frac{1}{F_h^+} = \frac{\tilde{U}}{\Omega h} \tag{14}$$

where h is the height of the synthetic jet outlet and $\tilde{U}$ is the time- and spatial-averaged synthetic jet exit velocity given by

$$\tilde{U} = \frac{2\Omega}{h} \int_0^h \int_0^{1/2\Omega} u(t, h)\, \mathrm{d}t\, \mathrm{d}h \tag{15}$$

Holman et al. [29] proposed that, when this quality is greater than about one, a synthetic jet is formed. In the case of full actuation ($C_\mu = 1.05 \times 10^{-3}$), the inverse of the Strouhal number is 3.86, and so (as is shown in Fig. 21) a jet is formed. If the jet strength is not high enough to reach the formation criteria, then the pair of vortices is ingested back into the slot during the inflow phase and no jet is formed. Figure 22 shows the evolution of the vorticity field in one actuation cycle for $C_\mu = 2.6 \times 10^{-4}$. The cycle starts with the outflow (Fig. 22a), in which the fluid is blown out of the actuator cavity and a pair of corotating vortices are formed at the synthetic jet outlet. The size and strength of the vortices increase as the outflow phase continues (see Figs. 22b and 22c) but not as strong as in the full actuation case. The outflow finishes in Fig. 22c, but the vortices are not detached and stay at the synthetic jet outlet. The inflow starts in Fig. 22d, in which the pair of corotating vortices start being sucked into the synthetic jet outlet. As the inflow continues (Figs. 22e and 22f), the vortices are slowly ingested into the synthetic jet as their size and strength decreases. Finally, the cycle is completed, as is shown in Fig. 22g, in which the pair of corotating vortices were completely ingested back into the slot. For this case, the inverse of the Strouhal number was ≈0.98, so the evolution shown in Fig. 22 is consistent with the theory of jet formation, and it is expected that the performance of the synthetic jet will be seriously affected for this operating condition.

3. Effects on Aerodynamic Properties

Figure 23a shows the evolution of C_m at $\alpha = 0°$, in which the actuator is active after 7.5 convective time units. The oscillation in the magnitude of the aerodynamic properties when there is no actuation is due to the vortex shedding. When the SS actuator is active, there is an increase in the pitchdown moment; conversely, there is a net

pitchup moment when the PS actuator is active. Figure 23b shows the effects of the actuator on the C_l for the same simulation. When the SS actuator is active, there is an increment of the lift coefficient, while there is a reduction when the PS actuator is active; similar observations were reported in the experimental measurements. The effect of the actuation on the drag coefficient at an angle of attack of 0° is shown in Fig. 24. The change in the drag is negligible, since the average C_d value before actuation is ≈0.016, while for the suction and PS actuation, it is ≈0.0157 and ≈0.0152, respectively; this observation is in agreement with the experimental results [9].

Another important observation is the change in the dominant frequencies in the evolution of the aerodynamic properties in which, before actuation, the shedding frequency is dominant, but with actuation, it is the actuation frequency that is dominant. A Fourier analysis of the moment coefficient evolution was performed to further analyze the effects of the trailing-edge geometry. Figure 25a shows the frequency spectrum of the SS moment coefficient evolution in which two primary peaks are observed in the frequency spectrum: at $F = 31.2\frac{U_\infty}{c}$ and at $F = 5.1\frac{U_\infty}{c}$. The first occurs at the actuation frequency F^+, while the other is at the shedding frequency S_t. In fact, S_t is shifted to a higher frequency compared with that for the unactuated case of 4.2. A similar analysis was performed on the PS actuation. In this case, the shedding frequency is highly reduced in comparison with the unactuated case (see Fig. 25b).

Since the stabilization of the wake was suppressed by rounding the trailing edge, a Fourier analysis of simulation results with a rounded trailing edge was also performed (See Fig. 26). With the rounded trailing edge, the shedding frequency in all cases occurs at $F \approx 4.2$. This result corroborates the effect of the trailing-edge geometry on the stabilization of the wake and the magnitude of the shedding frequency relative to the unactuated case. The effect of this small trailing-edge rounding on the time-averaged aerodynamic properties is otherwise negligible, as shown in Fig. 27.
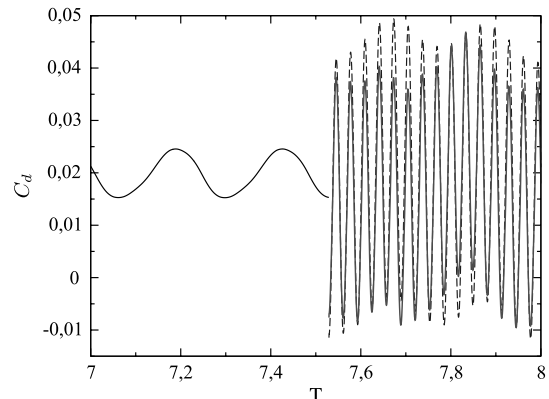

Fig. 24 Drag coefficient as a function of T (solid line: no actuation, dashed line: SS, solid line: PS).
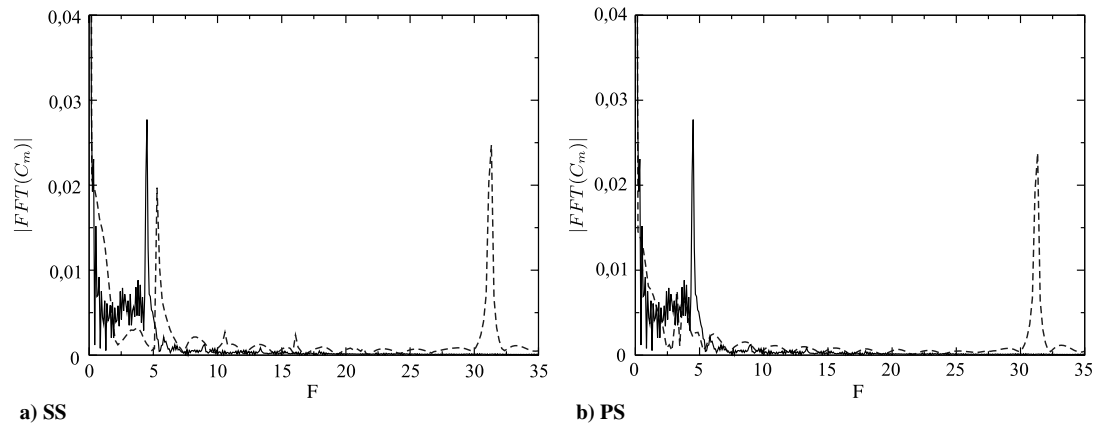
a) SS

b) PS

Fig. 25 Fourier transform of the evolution of C_m (solid line: no actuation, dashed line: actuation).
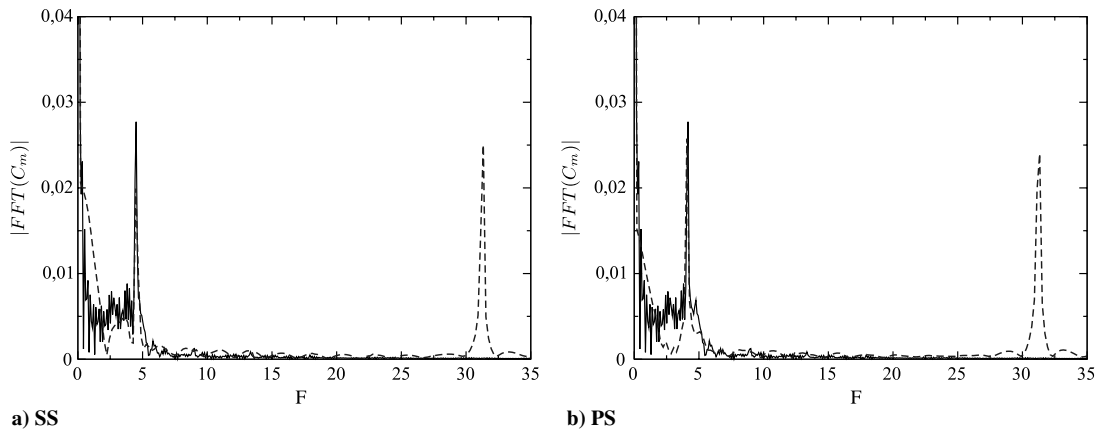

a) SS

b) PS

Fig. 26 Fourier transform of the evolution of C_m with rounded trailing edge (solid line: no actuation, dashed line: actuation).

Figure 28 shows the variation of the time-averaged pressure coefficient C_p along the airfoil due to full actuation at an angle of attack of 0°. Actuation influences the pressure distribution, especially at the trailing edge, where a spike in the pressure is induced by the actuation. The increment of C_p at full actuation, for both the suction and PS actuators, at $\frac{x}{c} = 0.95$ (position of the synthetic jet outlet) is about 0.9 relative to the unactuated case. Similar results

were reported by DeSalvo and Glezer [8] with the same actuators but on a different airfoil. This local reduction of the pressure is associated with the trapped vorticity and with a flow acceleration close to the trailing edge. Figure 29 shows the effect of the SS jet strength on the time-averaged pressure coefficient at an angle of attack of 0°. On the left, it is shown that as the level of actuation decreases, the area inside the C_p curve (hence C_l) decreases. Figure 29 (right) shows a
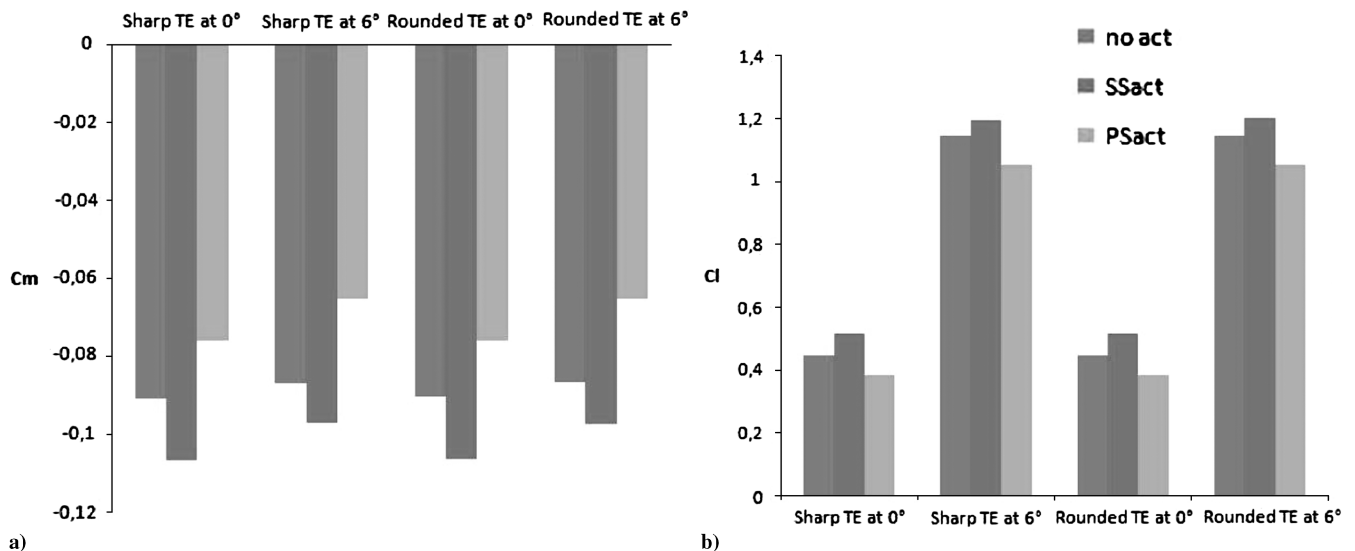

a)

b)

Fig. 27 Time-averaged aerodynamic properties for rounded and sharp trailing edges (TE: trailing edge, noact: no actuation, SSact: SS actuation, PSact: PS actuation).
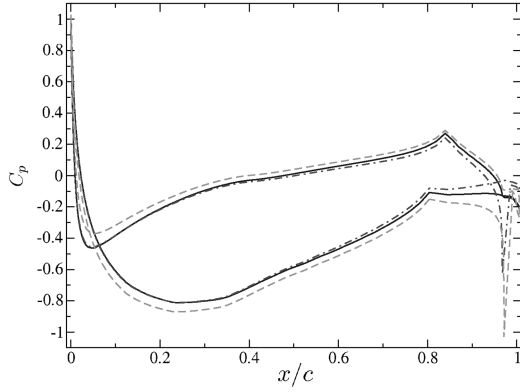
Fig. 28 Pressure coefficient at $\alpha = 0°$ (dashed line: actuation, solid line: no actuation).

detail of the C_p spike near the trailing edge caused by the actuation. It is clear that, for one-quarter of the full actuation, there is an important reduction of the effects of actuation on C_p: an observation that is in agreement with the synthetic jet formation analysis discussed in Sec. IV.B.2.

The effectiveness of the actuator can be quantified by computing the increase/decrease of the aerodynamic properties of the airfoil: in particular, the change in moment and lift coefficients (ΔC_m and ΔC_l, respectively). Figure 30 shows the effectiveness of the actuator (computational and experimental) in the range of -2 to $6°$ at full actuation. Since ΔC_m is a small quantity of $\mathcal{O}(10^{-4})$, it is very sensitive to the boundary condition parameter A, so that the performance of the detailed synthetic jet model could be improved by more precisely matching the experimental data.

V. Conclusions

A computational study of a modified NACA4415 with synthetic jet actuators close to the trailing edge was presented. For this purpose, an implementation of an EDDES turbulence model in a nearly kinetic energy-conserving code (CDPv2.3) was developed. In hybrid RANS/LES models, the transition from RANS to LES relies on the grid. A hybrid grid was generated with a structured grid close to the airfoil (RANS region) and unstructured grid elsewhere (LES and Euler regions). The mesh generation in the airfoil surface normal direction requires some prior knowledge of the flow, such as expected boundary-layer thickness and transition location. Using a panel method with integral boundary-layer representation was effective in determining these quantities, leading to a successful grid generation process. The EDDES implementation was tested on a flat-plate boundary-layer flow and in the flow around a NACA4415 airfoil; both tests showed satisfactory results in agreement with other numerical and experimental studies.

Numerical results of the baseline case for the aerodynamic properties (including C_d) are considered satisfactory. Regarding the time-averaged vorticity field in the near wake, computational results are acceptable in the size and magnitude of the recirculation regions. On the other hand, stronger concentrations of vorticity close to the airfoil surface were observed in the computational results that were attributed to higher resolution of the CFD in this part of the domain compared with the PIV measurements. Another important observation is that the modification of the airfoil (due to the actuators) moves the aerodynamic center $\approx 0.025c$ toward the trailing edge.

The simulation of the synthetic jet actuators was done with a detailed time-resolved model. Numerical results demonstrated the effects of the synthetic jets in the flow (especially in the trapped vorticity close to the trailing edge) and in the aerodynamic properties of the airfoil (specifically, C_l and C_m). The main effect of the

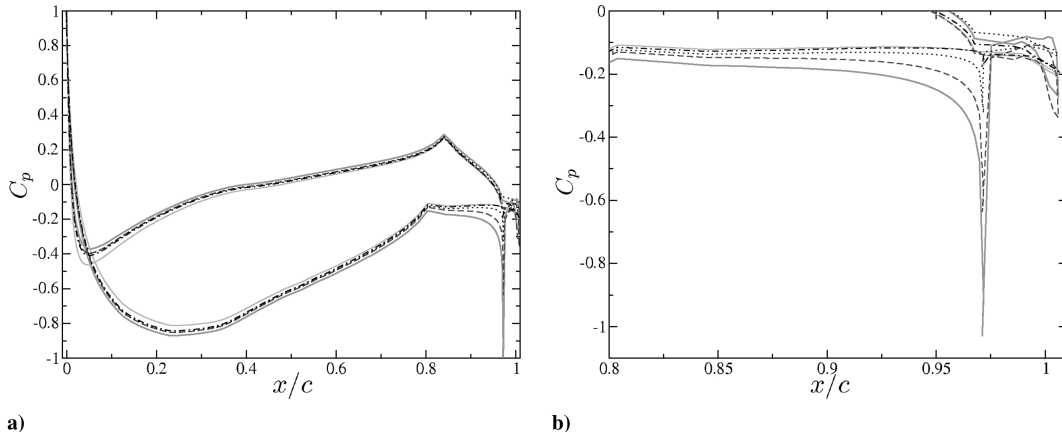a)   b)

Fig. 29 Pressure coefficient at $\alpha = 0°$ for different levels of SS actuation (solid lines: no and full actuation, dashed lines: intermediate actuation levels).
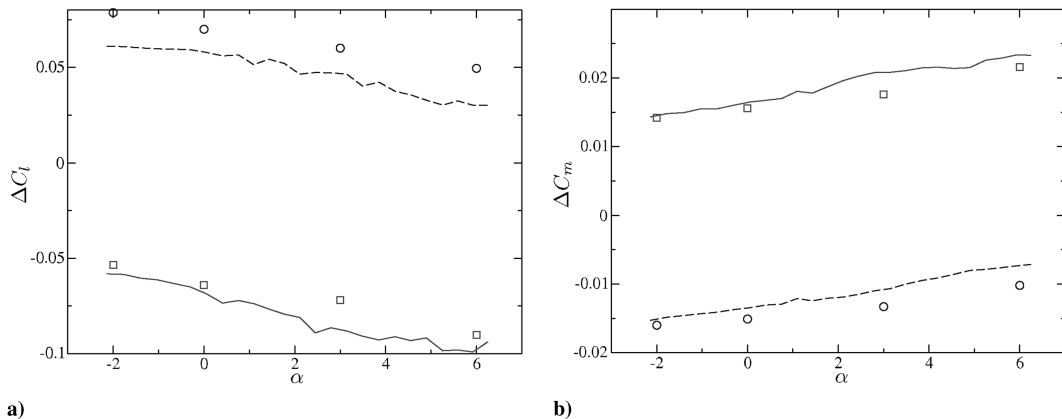

a)   b)

Fig. 30 ΔC_l as a function of α (○: SS comp, □: PS comp, solid line: PS experimental, dashed line: SS experimental).

actuation (observed on both experimental and computational results) on the time-averaged vorticity field is a bending of the separation shear layer from the actuator toward the airfoil surface, resulting in changes in the aerodynamic properties. The size and magnitude of the time-averaged vorticity field in the near wake are in good agreement with experimental PIV data that shows a downwash of the near wake for the SS actuation and an upwash of the near wake for the PS actuation. The instantaneous vorticity fields for the PS actuator showed a wake stabilization for a sharp trailing edge that was broken with a rounded trailing edge. A detailed analysis of the vorticity dynamics close to the synthetic jet outlet showed a synthetic jet formation for full actuation and a significant reduction of the synthetic jet formation for one-quarter of the full actuation. This observation is in agreement with a significant reduction of the pressure spike close to the synthetic jet outlet for $C_\mu = 2.6 \times 10^{-4}$.

The effects on the aerodynamic properties showed that full actuation of the SS actuator increases both the magnitude of the nosedown pitching moment and the lift force, while the PS actuator reduces the magnitude of the nosedown pitching moment and the lift force. These observations are in agreement with the experimental results. Trapped vorticity close to the trailing edge of the airfoil affects the pressure distribution along the airfoil, which is responsible for the aerodynamic property modifications. C_p curves showed a clear local suction peak close to the synthetic jet outlet for both PS and SS actuations. The effectiveness of the actuator was computed as increments/reductions of C_l and C_m. Errors of less than 10% were obtained between the experimental and computational results for ΔC_m and ΔC_l at full actuation, but this could be improved by more precisely matching the experimental data; that is, increase the precision of the boundary condition amplitude A. Since the actuators are located close to the trailing edge, there is an important influence of the precise trailing-edge geometry on the synthetic jet model prediction of S_t and the spanwise vorticity field in the wake. A Fourier analysis of the evolution of the moment coefficient corroborated the influence of the trailing-edge geometry in the shedding frequency. While a sharp trailing edge causes a shift in the shedding frequency for both SS and PS actuation, a rounded trailing edge did not show any influence of the actuation in the shedding frequency in comparison with the baseline case.

In the context of the AVOCET project, the present study provided detailed information about the controlled flow, which is not possible to measure in experiments such as the early evolution of the aerodynamic properties in an impulsive started flow. The set of CFD tools described in this paper has been integrated with the controller designed at the Georgia Institute of Technology to successfully perform controlled dynamic simulations.

Acknowledgments

References

[1] Greenblatt, D., and Wygnanski, I., "The Control of Flow Separation by Periodic Excitation," *Progress in Aerospace Sciences*, Vol. 36, No. 7, 2000, pp. 487–545.
doi:10.1016/S0376-0421(00)00008-7

[2] Seifert, A., Bachar, T., Koss, T., Shepshelovich, M., and Wygnanski, I., "Oscillatory Blowing, a Tool to Delay Boundary Layer Separation," *AIAA Journal*, Vol. 31, No. 11, 1993, pp. 2052–2060.
doi:10.2514/3.49121

[3] Soldati, A., and Monti, R. (eds.), *Turbulence Structure and Modulation*, Springer, New York, 2001, pp. 235–255.

[4] Seifert, A., Daraby, A., and Wygnanski, I., "Delay of Airfoil Stall by Periodic Excitation," *Journal of Aircraft*, Vol. 33, No. 4, 1996, pp. 691–698.
doi:10.2514/3.47003

[5] DeSalvo, M., and Glezer, A., "Aerodynamic Performance Modification at Low Angles of Attack by Trailing Edge Vortices," 2nd AIAA Flow Control Conference, AIAA Paper 2004-2118, 2004.

[6] Amitay, M., Smith, D., Kibens, V., Parekh, D., and Glezer, A., "Aerodynamic Flow Control over an Unconventional Airfoil Using Synthetic Jets Actuators," *AIAA Journal*, Vol. 39, No. 3, 2001, pp. 361–370.
doi:10.2514/2.1323

[7] Glezer, A., Amitay, M., and Honohan, A., "Aspects of Low and High Frequency Actuation for Aerodynamic Flow Control," *AIAA Journal*, Vol. 43, No. 7, 2005, pp. 1501–1511.
doi:10.2514/1.7411

[8] DeSalvo, M., and Glezer, A., "Control of Airfoil Aerodynamic Performance Using Distributed Trapped Vorticity," AIAA 45th Aerospace Sciences Meeting and Exhibit, AIAA Paper 2007-708, 2007.

[9] DeSalvo, M., and Glezer, A., "Airfoil Aerodynamic Performance Modification Using Hybrid Surface Actuators," AIAA 43th Aerospace Sciences Meeting and Exhibit, AIAA Paper 2005-0872, 2005.

[10] DeSalvo, M., Amitay, M., and Glezer, A., "Modification of the Aerodynamic Performance of Airfoil at Low Angle of Attack: Trailing Edge Trapped Vortices," AIAA Paper 2002-3165, 2002.

[11] Rumsey, C., "Successes and Challenges for Flow Control Simulations," *International Journal of Flow Control*, Vol. 1, No. 1, 2009, pp. 1–27.
doi:10.1260/1756-8250.1.1.1

[12] Raju, R., Aram, E., Mittal, R., and Cattafesta, L., "Simple Models of Zero-Net Mass-Flux Jets for Flow Control Simulations," *International Journal of Flow Control*, Vol. 1, No. 3, 2009, pp. 179–197.
doi:10.1260/175682509789877092

[13] Brzozowski, D., Culp, J., Kutay, A., Muse, J., and Glezer, A., "Closed-Loop Aerodynamic Flow Control of a Free Airfoil," AIAA 4th Flow Control Conference, AIAA Paper 2008-4323, 2008.

[14] Brzozowski, D., and Glezer, A., "Transient Separation Control Using Pulse-Combustion Actuation," AIAA Paper 2002-3166, 2002.

[15] Kutay, A., Culp, J., Muse, J., Brzozowski, D., Glezer, A., and Calise, A., "A Closed-Loop Flight Control Experiment Using Active Flow Control Actuators," 45th AIAA Aerospace Sciences Meeting and Exhibit, AIAA Paper 2007-0114, 2007.

[16] Muse, J., Kutay, A., Brzozowski, D., Calise, D., and Glezer, A., "Dynamic Flight Maneuvering Using Trapped Vorticity Flow Control," AIAA 46th Aerospace Sciences Meeting and Exhibit, AIAA Paper 2008-0522, 2008.

[17] Spalart, P., "Detached-Eddy Simulation," *Annual Review of Fluid Mechanics*, Vol. 41, No. 1, 2009, pp. 181–202.
doi:10.1146/annurev.fluid.010908.165130

[18] Spalart, P., "Strategies for Turbulence Modelling and Simulations," *International Journal of Heat and Fluid Flow*, Vol. 21, No. 3, 2000, pp. 252–263.
doi:10.1016/S0142-727X(00)00007-2

[19] Spalart, P., Deck, S., Shur, M., Squires, K., Strelets, M., and Travin, A., "A New Version of Detached-Eddy Simulation, Resistant to Ambiguous Grid Densities," *Theoretical and Computational Fluid Dynamics*, Vol. 20, No. 3, 2006, pp. 181–195.
doi:10.1007/s00162-006-0015-0

[20] Travin, A., Shur, M., Strelets, M., and Spalart, P., "Detached-Eddy Simulations Past a Circular Cylinder," *Flow, Turbulence and Combustion*, Vol. 63, Nos. 1–4, 2000, pp. 293–313.
doi:10.1023/A:1009901401183

[21] Riou, J., Garnier, E., Deck, S., and Basdevant, C., "Improvement of a Delayed-Detached Eddy Simulation Applied to Separated Flow Over Missile Fin," *AIAA Journal*, Vol. 47, No. 2, 2009, pp. 345–360.
doi:10.2514/1.37742

[22] Zwart, P., "The Integrated Space-Time Finite Volume Method," Ph.D. Thesis, Univ. of Waterloo, Waterloo, Ontario, Canada, 1999.

[23] Abbott, I., and Doenhoff, A. V., *Theory of Wing Sections*, Dover, New York, 1949, pp. 290–291.

[24] Bunge, U., Mockett, C., and Thiele, F., "Guidelines for Implementing Detached-Eddy Simulation Using Different Models," *Aerospace Science and Technology*, Vol. 11, No. 5, 2007, pp. 376–385.
doi:10.1016/j.ast.2007.02.001

[25] Shur, M., Spalart, P., Strelets, M., and Travin, A., "Detached-Eddy Simulation of an Airfoil at High Angle Of Attack," *4th International Symposium on Engineering Turbulence Modelling and Measurements*, edited by W. Rodi and D. Laurence, Elsevier Science, New York, 1999, pp. 669–678.

[26] Spalart, P., "Young-Person's Guide to DES grids," NASA TR CR-2001-211032, 2001.

[27] Adrian, R., "Particle-Imaging Techniques for Experimental Fluid Mechanics," *Annual Review of Fluid Mechanics*, Vol. 23, No. 1, 1991, pp. 261–304.

doi:10.1146/annurev.fl.23.010191.001401

[28] Westerweel, J., "Theoretical Analysis of the Measurement Precision in Particle Image Velocimetry," *Experiments in Fluids*, Vol. 29, Supplement 1, 2000, pp. S003–S012.
doi:10.1007/s003480070002

[29] Holman, R., Utturkar, Y., Mittal, R., Smith, B., and Cattafesta, L., "Formation Criterion for Synthetic Jets," *AIAA Journal*, Vol. 43, No. 10, 2005, pp. 2110–2116.
doi:10.2514/1.12033

F. Coton
Associate Editor